Additional processes and diagnostic variables in the CSIRO Environmental Modelling Suite

Mark E. Baird[1]

[1]CSIRO Environment, Hobart, Australia

February 29, 2024

0.1 Outline of document

A comprehensive description of the EMS optical and biogeochemical version B3p0 is given in Baird et al. (2020), as published in 2020. This document provides scientific description of processes added since this work (Sec. 2), as well as the calculation of diagnostic variables that were not described in Baird et al. (2020), including simulated true color (Sec. 3).

1 Water column - sediment fluxes

The sediment model used in EMS is evaluated on a stretched Eulerian coordinate system for which the equations of the change in concentration of particulate and dissolved tracers due to vertical fluxes are given in Margvelashvili (2009). Here we give the equations in term of a fixed sediment-water column interface. The processes affecting vertical fluxes are settling rate, sediment deposition (entraining water column pore-water), resuspension releasing porewater into the water column) as well as diffusive fluxes. We define δh as the change in sediment height, with $\delta h > 0$ resulting from deposition causing entrainment of water in the sediments, while $\delta h < 0$ is the erosion of surface sediments and release of porewaters into the sediments.

For a dissolved tracer, C, with water column, C_w and sediment, C_w, concentrations, and a sediment porosity, ϕ, the sediment - water flux is given by:

$$F_C = D\left(C_w - C_s\right) + \delta h C_w + \delta h \phi C_s \tag{1}$$

and D is the diffusion coefficient of the interface.

2 Processes added after GMD submission

2.1 Dimethyl sulfide (DMS)

Dimethyl sulfide (DMS) is produced through the degradation of organic matter and through exchange (typically as a loss) to the atmosphere. We consider the first stage of organic matter breakdown to be from a living form (such as phytoplankton / seagrass) to a suspended particulate matter in the water column, a process that does not release DMS. All DMS is released in the next stage, the breakdown of labile detritus to refractory detritus:

$$\frac{\partial \mathcal{D}}{\partial t} = \varphi_{Red,DMS}\, r_{Red} D_{Red} + \varphi_{Atk,DMS}\, r_{Atk} D_{Atk} \tag{2}$$

where $\mathcal{D}$ is the concentration of DMS is the water column; D_{Red} is the mass of the labile detritus at the Redfield ratio (C:N:P = 106:16:1 mol:mol:mol); r_{Red} is the breakdown rate of labile detritus at the Redfield ratio; $\varphi_{Red,DMS}$ is stoichiometric coefficient between labile detritus at the Redfield ratio and DMS; D_{Atk} is the mass of the labile detritus at the Atkinson ratio (C:N:P = 550:30:1 mol:mol:mol); r_{Atk} is the breakdown rate of labile detritus at the Atkinson ratio; and $\varphi_{Atk,DMS}$ is stoichiometric coefficient between labile detritus at the Atkinson ratio and DMS. No DMS is released during the breakdown of refractory detritus or dissolved organic matter.

Air-sea gas exchange for DMS is calculated using a transfer coefficient, $k_{\mathcal{D}}$, given by (Goddijn-Murphy et al., 2012):

$$k_{\mathcal{D}} = \frac{\max[(2.1u_{10} - 2.8), 0.0]}{360000} * \sqrt{\frac{600}{Sc}} \tag{3}$$

where u_{10} is the short-term steady wind at 10 m above the sea surface [m s^{-1}], the Schmidt number, Sc, is the ratio of the diffusivity of momentum and that of the exchanging gas. Finally, a conversion factor of 360000 m s^{-1} (cm $hr^{-1})^{-1}$ is used.

The Schmidt number is calculated as Saltzman et al. (1993):

$$Sc = 2674 - 147.12T + 3.726T^2 - 0.038T^3 \tag{4}$$

where T is the surface temperature.

The change in concentration of DMS in the surface layer due to a sea-air DMS flux (positive from sea to air) is given by:

$$\frac{\partial[\mathcal{D}]}{\partial t} = k_{\mathcal{D}}\mathcal{D}/h \tag{5}$$

where $k_{\mathcal{D}}$ is the transfer coefficient for DMS (Eq. 3), $\mathcal{D}$ is the dissolved DMS concentration in the surface waters, and h is the thickness of the surface layer of the model into which sea-air flux exchanges.

*Notes: No breakdown of DMS in sediments, all benthic plants are living, and first stage of breakdown does not release DMS.

2.2 Anammox

Anaerobic ammonium oxidation (anammox) is a globally important microbial process of the nitrogen cycle that takes place in many natural environments. It is the combination of nitrite and ammonium to make water and di-nitrogen gas. As the model does not explicitly represent nitrite, we assume that anammox is the combination of nitrate and ammonium to make water and di-nitrogen gas:

Variable	Symbol	Units
Ammonium concentration	$[NH_4]$	mg N m^{-3}
Nitrate concentration	$[NO_3]$	mg N m^{-3}
Dissolved oxygen concentration	$[O_2]$	mg O m^{-3}

Table 1: State and derived variables for anammox.

Description	Symbol	Units
Maximum rate of anammox in the water column	$r_{ana,wc}$	0.1 d^{-1}
Maximum rate of anammox in the sediment	$r_{ana,sed}$	0.1 d^{-1}
Oxygen half-saturation constant for nitrification	$K_{O_2,ana}$	500 mg O m^{-3}

Table 2: Constants and parameter values used in the anammox process.

$$\text{Anammox} : 2H^+ + NH_4^+ + NO_3^- \longrightarrow N_2 + 3H_2O \tag{6}$$

The excess oxygen molecule in nitrate compared to nitrate results in the generation of 3 water molecules, and the need for two hydrogen ions in the reactants. Because neither hydrogen ions nor oxygen bound in water molecules are included in the model's mass budget, anammox results in a loss of DIN and oxygen from the model.

We assume that anammox proceeds at a rate proportional the minimum concentration of the two reactants:

$$\frac{\partial DIN}{\partial t} = r_{ana} \min\left[[NH_4], [NO_3]\right] \exp\left(-[O_2]/K_{O_2,ana}\right) \tag{7}$$

where r_{ana} is the temperature-dependent rate coefficient for anammox. The exponential term on the right side of Eq. 7 results in the anammox proceeding at its maximum rate when the dissolved oxygen concentration is zero. The parameter $K_{O_2,ana}$ is the oxygen concentration at which anammox proceeds at $1/e$, or 37 % of its maximum rate. At oxygen saturation anammox is greatly reduced.

(8)

$$\frac{\partial[\mathrm{NH_4}]}{\partial t} = -\frac{1}{2} r_{ana} \min\left[[\mathrm{NH_4}], [\mathrm{NO_3}]\right] \exp\left(-[\mathrm{O_2}]/K_{\mathrm{O_2},ana}\right) \quad (9)$$

$$\frac{\partial[\mathrm{NO_3}]}{\partial t} = -\frac{1}{2} r_{ana} \min\left[[\mathrm{NH_4}], [\mathrm{NO_3}]\right] \exp\left(-[\mathrm{O_2}]/K_{\mathrm{O_2},ana}\right) \quad (10)$$

$$\frac{\partial[\mathrm{O_2}]}{\partial t} = -\frac{3}{2}\frac{16}{14} r_{ana} \min\left[[\mathrm{NH_4}], [\mathrm{NO_3}]\right] \exp\left(-[\mathrm{O_2}]/K_{\mathrm{O_2},ana}\right) \quad (11)$$

Table 3: Equations for Anammox.

3 Diagnostic outputs

Name	Units	Description
Absorption at 440 nm (at_440)	m^{-1}	Total absorption due to clear water, CDOM, microalgae and suspended sediments at 440 nm.
Scattering at 550 nm (bt_550)	m^{-1}	Total scattering due to clear water, microalgae and suspended sediments at 550 nm.
Vertical attenuation at 490 nm (Kd_490)	m^{-1}	Vertical attenuation (along z axis not along zenith angle) of light at 490 nm.
Average PAR in layer (PAR)	mol photon m^{-2} s^{-1}	Mean scalar photosynthetically available radiation (400 - 700 nm) within the layer.
Downwelling PAR (PAR_z)	mol photon m^{-2} s^{-1}	Mean downwelling photosynthetically available radiation (400 - 700 nm) at the top of each layer (i.e. on z_grid not z_centre)
Light intensity above seagrass (EpiPAR_sg)	mol photon m^{-2} d^{-1}	Mean downwelling photosynthetically available radiation (400 - 700 nm) above seagrass canopy.
Light intensity above sediment layer (EpiPAR)	mol photon m^{-2} d^{-1}	Mean downwelling photosynthetically available radiation (400 - 700 nm) at the sediment-water interface.
Vertical attenuation of heat (K_heat)	m^{-1}	Vertical attenuation (along z axis not along zenith angle) of heat energy.
Remote-sensing reflectance (R_X)	sr^{-1}	Remote-sensing reflectance at wavelength XXX nm, $R_{rs,X}$. R_{rs} is the ratio of water-leaving radiance (i.e. per solid angle) to the incoming solar irradiance (i.e. from all directions).
Satellite chlorophyll (OC*)	mg m^{-3}	Output of band ratio cholorophyll algorithms (OC3M, OC3V)

Table 4: Long name (and variable name) in model output files, units, and description of optical diagnostic variables. Unless otherwise stated quantities are cell centred vertical averages.

Name	Units	Description
Bicarbonate (HCO3)	mmol m^{-3}	Concentration of bicarbonate ions [HCO_3^-] calculated from carbon chemistry equlibra at water column values of T, S, DIC and A_T.
Carbonate (CO3)	mmol m^{-3}	Concentration of carbonate ions [CO_3^{2-}] calculated from carbon chemistry equlibra at water column values of T, S, DIC and A_T.
Aragonite saturation state (omega_ar)	-	Aragonite saturation state (Ω_a) calculated from DIC, A_T, T and S assuming the carbonate system is at equilibrium.
Oxygen % saturation (Oxy_sat)	%	Dissolved oxygen concentration as a percentage of the saturation concentration at atmospheric pressure and local T and S.
pH (PH)	$\log_{10}$ mol m^{-3}	pH based on [H^+] calculated from carbon chemistry equlibra at water column values of T, S, DIC and A_T.
Sea-air CO_2 flux (CO2_flux)	mg C m^{-2} s^{-1}	Flux of carbon from sea to air (positive from sea to air). The value is given in the layer in which it was deposited (must be thicker than 20 cm), but still represents an areal flux.
Sea-air O_2 flux (O2_flux)	mg O m^{-2} s^{-1}	Flux of oxygen from sea to air (positive from sea to air). The value is given in the layer in which it was deposited (must be thicker than 20 cm), but still represents an areal flux.
Delta pCO_2 (dco2star)	ppmv	Partial pressure of CO_2 in the ocean minus that of the atmosphere (396 ppmv).
Oceanic pCO_2 (pco2surf)	ppmv	Partial pressure of CO_2 in the ocean.

Table 5: Long name (and variable name) in model output files, units, and description of gas diagnostic variables. Unless otherwise stated quantities are cell centred vertical averages.

Name	Units	Description
Total C, N, P (TC, TN, TP)	mg m^{-3}	Sum of dissolved and particulate C, N, and P.
Total chlorophyll a (Chl_a_sum)	mg m^{-3}	Sum of chlorophyll concentration of the four microalgae types ($\sum nc_i V_i$).
Ecology Fine Inorganics (EFI)	kg m^{-3}	Sum of inorganic components (see `ecology_setup.txt` for those specified in the code) used for TSS-dependent calculations such as phosphorus absorption.
Ecology Particulate Organics (EPO)	kg m^{-3}	Weight of carbon in microalgae, zooplankton, and particulate detritus.
Large phytoplankton net production (PhyL_N_pr)	mg C m^{-3} d^{-1}	Rate of large phytoplankton organic matter synthesis from inorganic constituents.
Small phytoplankton net production (PhyS_N_pr)	mg C m^{-3} d^{-1}	Rate of small phytoplankton organic matter synthesis from inorganic constituents.
Trichodesmium net production (Tricho_N_pr)	mg C m^{-3} d^{-1}	Rate of *Trichodesmium* organic matter synthesis from inorganic constituents.
Microphytobenthos net production (MPB_N_pr)	mg C m^{-3} d^{-1}	Rate of microphytobenthos organic matter synthesis from inorganic constituents.
Total phytoplankton net production (P_prod)	mg C m^{-3} d^{-1}	Rate of total phytoplankton organic matter synthesis from inorganic constituents.
Large zooplankton removal rate from small zooplankton	mg C m^{-3} d^{-1}	Rate of carnivory of large zooplankton on small zooplankton.
Small zooplankton removal rate from small phytoplankton	mg C m^{-3} d^{-1}	Secondary production of small zooplankton.
Large zooplankton removal rate from large phytoplankton	mg C m^{-3} d^{-1}	Secondary production of large zooplankton.
Zooplankton total grazing (Z_grazing)	mg C m^{-3} d^{-1}	Total secondary pelagic production - feeding of both zooplankton classes on phytoplankton.
N_2 fixation (Nfix)	mg N m^{-3} s^{-1}	Nitrogen fixation by *Trichodesmium*.
Trichodesmium settling velocity (Tricho_sv)	m s^{-1}	Vertical sinking rate of *Trichodesmium*.

Table 6: Long name (and variable name) in model output files, units, and description of pelagic diagnostic variables.

Name	Units	Description
Total epibenthic C, N, P (EpiTC, EpiTN, EpiTP)	mg m^{-2}	Sum of C, N, and P in epibenthic plants and corals.
Halophila production (SGH_N_pr)	g N m^{-2} d^{-1}	Gross production of nitrogen in *Halophila*, where N fluxes are not accounted for in respiration.
Halophila growth rate (SGH_N_gr)	s^{-1}	Turnover time of above-ground *Halophila* biomass.
Seagrass growth rate (SG_N_gr)	s^{-1}	Turnover time of above-ground *Zostera* biomass.
Seagrass production (SG_N_pr)	g N m^{-2} d^{-1}	Gross production of nitrogen in *Zostera*, where N fluxes are not accounted for in respiration.
Seagrass shear mort. (SG_shear_mort)	d^{-1}	Loss rate of seagrass due to shear stress mortality.
Deep SG shear mort. (SGD_shear_mort)	d^{-1}	Loss rate of deep seagrass due to shear stress mortality.
Halophila shear mort. (SGH_shear_mort)	d^{-1}	Loss rate of *Halophila* due to shear stress mortality.
Deep seagrass growth rate (SGD_N_gr)	s^{-1}	Turnover time of above-ground deep seagrass biomass.
Deep seagrass production (SGD_N_pr)	g N m^{-2} d^{-1}	Gross production of nitrogen in deep seagrass, where N fluxes are not accounted for in respiration.
Macroalgae growth rate (MA_N_gr)	s^{-1}	Turnover time of macroalgae biomass.
Macroalgae production (MA_N_pr)	g N m^{-2} d^{-1}	Gross production of nitrogen in macroalgae, where N fluxes are not accounted for in respiration.

Table 7: Long name (and variable name) in model output files, units and description of benthic diagnostic variables.

Name	Units	Description
Coral inorganic supply (Coral_IN_up)	mg N m^{-2} s^{-1}	Flux of dissolved inorganic nitrogen into coral polyps from the water column, absorbed by zooxanthellae. Note that the flux is averaged over the whole grid cell, while the fraction of the bottom that is responsible for this uptake is given by A_{eff} (Eq. **??**)
Coral organic supply (Coral_ON_up)	mg N m^{-2} s^{-1}	Flux of particulate organic nitrogen into coral polyps from the water column, consumed by the coral host. See coral organic supply.
Net calcification (Gnet)	mg C m^{-2} s^{-1}	Net calcification (calcification minus dissolution) at the sediment-water column interface leading to a change in the water column properties.
Rubisco activity, $a^*_{Q_{ox}}$ (CS_tempfunc)	-	Activity of the Ribulose-1,5-bisphosphate carboxylase/oxygenase (RuBisCO) enzyme based on the seabed temperature anomaly from a spatially-varying maximum summer temperature. It takes a value of 1 below the summer time maximum, and 0 at 2°C above (Eq. **??**).
Coral bleaching rate (CS_bleach)	d^{-1}	Loss rate of zooxanthellae due to reactive oxygen stress.
Coral mucus release (mucus)	mg N m^{-2} s^{-1}	Release rate of organic matter (at the Redfield ratio) due to polyp and symbiont moratlity terms, excluding those due to reactive oxygen stress driven expulsion.

Table 8: Long name (and variable name) in model output files, units and description of coral diagnostic variables.

Name	Units	Description
Porosity (porosity_sed, ϕ)	-	Fraction of a layer by volume that is occupied by water. Calculated from the the sum of the mass divided by Sediment density of each of the particulate components, compared to that of water.
Sea-water sed * flux (*_sedflux)	mg m^{-2}	The sea-water (+ve into water) flux of diffused tracer * calculated by the ecological process `diffusion_epi`. This diffusion rate, typically much quicker than the sediment model, accounts for the fast diffusion between the top sediment layer and the bottom
Sea-water sed * flux (*_fluxsedi_inst)	mg m^{-2}	The sea-water (+ve into water) flux of diffused tracer * calculated by the sediment model. This calculation includes, entrainment of porewaters during sediment deposition, loss of porewater during erosion, and a slow diffusion rate.
Denitrfication flux (Den_fl)	mg N m^{-2} d^{-1} $layer^{-1}$	Denitrification rate, specified per layer per m^2 (rather than per m^3) so that the depth-integrated denitrification rate can be calculated by summing each layer without knowing the thickness of each layer (that varies with time).

Table 9: Long name (and variable name) in model output files, units and description of sediment model diagnostic variables.

3.1 Diagnostic age tracer

Tracer 'age' is a diagnostic tracer (Monsen et al., 2002; Macdonald et al., 2009) use to quantify the spatially-resolved residence time of water in different regions. The age tracer, τ, is advected and diffused by the hydrodynamic model using the same numerical schemes as other tracers such as salinity. When inside the region of interest, the age increases at the rate of 1 d d^{-1}. When the age tracer is outside the region of interest, its age decays (or anti-ages) at the rate of Φ d^{-1}. Thus, the local rate of change over the whole domain is given by:

$$\frac{\partial \tau}{\partial t} = 1 \tag{12}$$

$$\frac{\partial \tau}{\partial t} = -\Phi\tau \qquad \text{outside ageing region} \tag{13}$$

$$\tag{14}$$

In some applications the age is held to zero outside the region to represent time since water moved within the area of interested (such as the surface mixed layer (Baird et al., 2006)). For more information see Mongin et al. (2016).

3.2 Remote-sensing reflectance

3.2.1 Backscattering

Backscattering. In addition to the IOPs calculated above, the calculation of remote-sensing reflectance uses a backscattering coefficient, b_b, which has a component due to pure seawater, and a component due to algal and non-algal particulates. The backscattering ratio is a coarse resolution representation of the volume scattering function, and is the ratio of the forward and backward scattering.

The backscattering coefficient for clear water is 0.5, a result of isotropic scattering of the water molecule.

For inorganic particles, backscattering can vary between particle mineralogies, size, shape, and at different wavelengths, resulting, with spectrally-varying absorption, in the variety of colours that we see from suspended sediments. Splitting sediment types by mineralogy only, the backscattering ratio for carbonate and non-carbonate particles is given in Table 10.

The backscatter due to phytoplankton is approximately 0.02. To account for a greater backscattering ratio, and therefore backscatter, at low wavelengths (Fig. 4 of Vaillancourt et al. (2004)), we

	Wavelength [nm]								
	412.0	440.0	488.0	510.0	532.0	595.0	650.0	676.0	715.0
Carbonate	0.0209	0.0214	0.0224	0.0244	0.0216	0.0201	0.0181	0.0170	0.0164
Terrestrial	0.0028	0.0119	0.0175	0.0138	0.0128	0.0134	0.0048	0.0076	0.0113

Table 10: Particulate backscattering ratio for carbonate and non-carbonate minerals based on samples at Lucinda Jetty Coastal Observatory, a site at the interface on carbonate and terrestrial bottom sediment (Soja-Woźniak et al., 2019).

linearly increased the backscatter ratio from 0.02 at 555 nm to 0.04 at 470 nm. Above and below 555 nm and 470 nm respectively the backscatter ratio remained constant.

The total backscatter then becomes:

$$b_{b,\lambda} = \tilde{b}_w b_{w,\lambda} + b^*_{bphy,\lambda} n + \tilde{b}_{b,NAP_{non-CaCO_3},\lambda} c_1 NAP_{\text{non-CaCO}_3} + \tilde{b}_{b,NAP_{CaCO_3},\lambda} c_2 NAP_{\text{non-CaCO}_3} NAP_{\text{CaCO}_3} \quad (15)$$

where the backscatter ratio of pure seawater, $\tilde{b}_w$, is 0.5, n is the concentration of cells, and for particulate matter (NAP and detritus), $\tilde{b}_{b,NAP,\lambda}$, is variable (Table 10) and the coefficients c_1 and c_2 come from the total scattering equations above.

The particulate component of total scattering for phytoplankton is strongly related to cell carbon (and therefore cell size) and the number of cells (Vaillancourt et al., 2004):

$$b^*_{bphy,\lambda} = 5 \times 10^{-15} m_C^{1.002} \quad (R^2 = 0.97) \quad (16)$$

where m_C is the carbon content of the cells, here in pg cell^{-1}.

3.2.2 Water column contribution to remote-sensing reflectance

The ratio of the backscattering coefficient to the sum of backscattering and absorption coefficients for the water column, u_λ, is:

$$u_\lambda = \sum_{z'=1}^{N} \frac{w_{\lambda,z'} b_{b,\lambda,z'}}{a_{\lambda,z'} + b_{b,\lambda,z'}} \quad (17)$$

where $w_{\lambda,z'}$ is a weighting representing the component of the remote-sensing reflectance due to the absorption and scattering in layer number z', and N is the number of layers.

The weighting fraction in layer z' is given by:

$$w_{\lambda,z'} = \frac{1}{z_1 - z_0}\left(\int_0^{z_1} \exp\left(-2K_{\lambda,z}\right) dz - \int_0^{z_0} \exp\left(-2K_{\lambda,z}\right) dz\right) \tag{18}$$

$$= \frac{1}{z_1 - z_0}\int_{z_0}^{z_1} \exp\left(-2K_{\lambda,z}\right) dz \tag{19}$$

where K_λ is the vertical attenuation coefficient at wavelength λ described above, and the factor of 2 accounts for the pathlength of both downwelling and upwelling light. The integral of $w_{\lambda,z}$ to infinite depth is 1. In areas where light reaches the bottom, the integral of $w_{\lambda,z}$ to the bottom is less than one, and bottom reflectance is important (see Sec. 3.2.3).

The below-surface remote-sensing reflectance, r_{rs}, is given by:

$$r_{rs,\lambda} = g_0 u_\lambda + g_1 u_\lambda^2 \tag{20}$$

where $g_0 = 0.0895$ sr^{-1} (close to $1/4\pi$) and $g_1 = 0.1247$ sr^{-1} are empirical constants for the nadir-view in oceanic waters (Lee et al., 2002; Brando et al., 2012), and these constants result in a change of units from the unitless u to a per unit of solid angle, sr^{-1}, quantity $r_{rs,\lambda}$.

The above-surface remote-sensing reflectance, through rearranging Lee et al. (2002), is given by:

$$R_{rs,\lambda} = \frac{0.52 r_{rs,\lambda}}{1 - 1.7 r_{rs,\lambda}} \tag{21}$$

At open ocean values, $R_{rs} \sim 0.06u$ sr^{-1}. Thus if total backscattering and absorption are approximately equal, $u = 0.5$ and $R_{rs} \sim 0.03$ sr^{-1}.

3.2.3 Benthic contribution to remote-sensing reflectance

In the water column optical (Sec 3.2.2), the calculation of remote-sensing reflectance required the contribution to water-leaving irradiance from bottom reflection. In order to calculate the importance of bottom reflectance, the integrated weighting of the water column must be calculated (Sec. 3.2.2), with the remaining being ascribed to the bottom. Thus, the weighting of the bottom reflectance as a component of surface reflectance is given by:

$$w_{\lambda,bot} = 1 - \frac{1}{z_{bot}}\int_0^{z_{bot}} \exp\left(-2K_{\lambda,z'}\right) dz' \tag{22}$$

where K_λ is the attenuation coefficient at wavelength λ described above, the factor of 2 accounts for the pathlength of both downwelling and upwelling light.

The bottom reflectance between 400 and 800 nm of $\sim$ 100 substrates (including turtles and giant clams!) have been measured on Heron Island using an Ocean Optics 2000 (Roelfsema and Phinn, 2012; Leiper et al., 2012). The data for selected substrates are shown in Fig 3 of Baird et al. (2016). When the bottom is composed of mixed communities, the surface reflectance is weighted by the fraction of the end members visible from above, with the assumption that the substrates are layered from top to bottom by macroalgae, seagrass (*Zostera* then *Halophila*), corals (zooxanthellae then skeleton), benthic microalgae, and then sediments. Since the sediment is sorted in the simulation by the sediment process, the sediments are assumed to be well mixed in surface sediment layer. Implicit in this formulation is that the scattering of one substrate type (i.e. benthic microalgae) does not contribute to the relectance of another (i.e. sand). In terms of an individual photon, it implies that if it first intercepts substrate A, then it is only scattered and/or absorbed by A.

Calculation of bottom fraction.

The fraction of the bottom taken up by a benthic plant of biomass B is $A_{eff} = 1-\exp(-\Omega_B B)$, with $\exp(-\Omega_B B)$ uncovered. Thus the fraction of the bottom covered by macroalgae, seagrass (Zostera then shallow and deep Halophila) and corals polyps is given by:

$$f_{MA} = 1 - \exp(-\Omega_{MA} MA) \tag{23}$$

$$f_{SG} = (1 - f_{MA})\,(1 - \exp(-\Omega_{SG} SG)) \tag{24}$$

$$f_{SGH} = (1 - f_{MA} - f_{SG})\,(1 - \exp(-\Omega_{SGH} SGH)) \tag{25}$$

$$f_{SGD} = (1 - f_{MA} - f_{SG} - f_{SGH})\,(1 - \exp(-\Omega_{SGD} SGD)) \tag{26}$$

$$f_{polyps} = (1 - f_{MA} - f_{SG} - f_{SGH} - f_{SGD})\,(1 - \exp(-\Omega_{CH} CH)) \tag{27}$$

Of the fraction of the bottom taken up by the polyps, f_{polyps}, zooxanthellae are first exposed. Assuming the zooxanthellae are horizontally homogeneous, the fraction taken up by the zooxanthellae is given by:

$$f_{zoo} = \min[f_{polyps}, \frac{\pi}{2\sqrt{3}} n\pi r_{zoo}^2] \tag{28}$$

where πr^2 is the projected area of the cell, n is the number of cells, and $\pi/(2\sqrt{3}) \sim 0.9069$ accounts for the maximum packaging of spheres. Thus the zooxanthellae can take up all the polyp area. The fraction, if any, of the exposed polyp area remaining is assumed to be coral skeleton:

$$f_{skel} = f_{polyps} - \min[f_{polyps}, \frac{\pi}{2\sqrt{3}} n\pi r_{zoo}^2] \tag{29}$$

The benthic microalgae overlay the sediments. Following the zooxanthellae calculation above, the fraction taken up by benthic microalgae is given by:

$$f_{MPB} = \min[(1 - f_{MA} - f_{SG} - f_{SGH} - f_{SGD} - f_{polyps}), \frac{\pi}{2\sqrt{3}} n\pi r_{MPB}^2] \tag{30}$$

Finally, the sediment fractions are assigned relative to their density in the surface layer, assuming the finer fractions overlay gravel:

$$M = Mud_{\mathrm{CaCO_3}} + Sand_{\mathrm{CaCO_3}} + Mud_{\mathrm{non-CaCO_3}} + Sand_{\mathrm{non-CaCO_3}} + FineSed + Dust \tag{31}$$

$$f_{CaCO_3} = (1 - f_{MA} - f_{SG} - f_{SGH} - f_{SGD} - f_{polyps} - f_{MPB}) \left(\frac{Mud_{\mathrm{CaCO_3}} + Sand_{\mathrm{CaCO_3}}}{M} \right) \tag{32}$$

$$f_{non-CaCO_3} = (1 - f_{MA} - f_{SG} - f_{SGH} - f_{SGD} - f_{polyps} - f_{MPB}) \left(\frac{Mud_{\mathrm{non-CaCO_3}} + Sand_{\mathrm{non-CaCO_3}}}{M} \right) \tag{33}$$

$$f_{FineSed} = (1 - f_{MA} - f_{SG} - f_{SGH} - f_{SGD} - f_{polyps} - f_{MPB}) \left(\frac{FineSed + Dust}{M} \right) \tag{34}$$

with the porewaters not being considered optically-active. Now that the fraction of each bottom type has been calculated, the fraction of backscattering to absorption plus backscattering for the benthic surface as seen just below the surface, $u_{bot,\lambda}$, is given by:

$$\begin{aligned} u_{bot,\lambda} \quad = \quad & w_{\lambda,bot}(f_{MA}\rho_{MA,\lambda} \\ & + f_{SG}\rho_{SG,\lambda} \\ & + f_{SGH}\rho_{SGH,\lambda} \\ & + f_{SGD}\rho_{SGD,\lambda} \\ & + f_{zoo}\frac{b_{zoo,\lambda}}{a_{zoo,\lambda} + b_{zoo,\lambda}} \\ & + f_{skel}\rho_{skel,\lambda} \\ & + f_{MPB}\frac{b_{MPB,\lambda}}{a_{MPB,\lambda} + b_{MPB,\lambda}} \\ & + f_{\mathrm{CaCO_3}}\rho_{\mathrm{CaCO_3},\lambda} + f_{non-\mathrm{CaCO_3}}\rho_{non-\mathrm{CaCO_3},\lambda} + f_{FineSed}\rho_{non-\mathrm{CaCO_3},\lambda}) \end{aligned} \tag{35}$$

where the absorption and backscattering are calculated as given in Sec. **??**, and ρ is the measured bottom refectance of each end member (Dekker et al., 2011; Hamilton, 2001; Reichstetter et al., 2015).

For the values of surface reflectance for sand and mud from Heron Island (Roelfsema and Phinn, 2012; Leiper et al., 2012), and microalgal optical properties calculated as per Sec. **??**, a ternary plot can be used to visualise the changes in true colour with sediment composition (Fig 13 of Baird et al. (2016)).

It is important to note that while the backscattering of light from the bottom is considered in the model for the purposes of calculating reflectance (and therefore comparing with observations), it is

not included in the calculation of water column scalar irradiance, which would require a radiative transfer model (Mishchenko et al., 2002).

3.3 Simulated radiometer band response to hyperspectral signal.

Optical sensors quantify energy fluxes over a range of wavelengths (called a waveband). For example, the third ocean colour band on the OCLI sensor aboard Sentinel-3B has a maximum response at 443 nm, with a Gaussian shape with a full width at maximum height (FWMH) of 10 nm (Fig. 1). To determine for a given model hyperspectral reflectance the reflectance that would be measured by a sensor within a band b, $R_{sen,b}$ we use:

$$R_{sen,b} = \frac{\int R_{mod,\lambda} s_{b,\lambda} d\lambda}{\int s_{b,\lambda} d\lambda} \tag{36}$$

where $s_{b,\lambda}$ is the spectral response of band b at wavelength λ normalised to the maximum response, and $R_{mod,\lambda}$ is the reflectance of the model at wavelength λ.

Fig. 2 shows for Lucinda Jetty Coastal Observatory, a modelled spectrally-resolved remote-sensing reflectance and the equivalent remote-sensing reflectance for a selection of MODIS, Sentinel-3B and Himarawi8 bands. Approximating the band response as the remote-sensing reflectance at the central wavelength is a good approximation for Sentinel-3B and MODIS Aqua bands. However, the shortcomings of the broad width Himarawi8 band spectral response is overcome by providing an integrated remote-sensing reflectance, normalised by the response of band (Eq. 36).

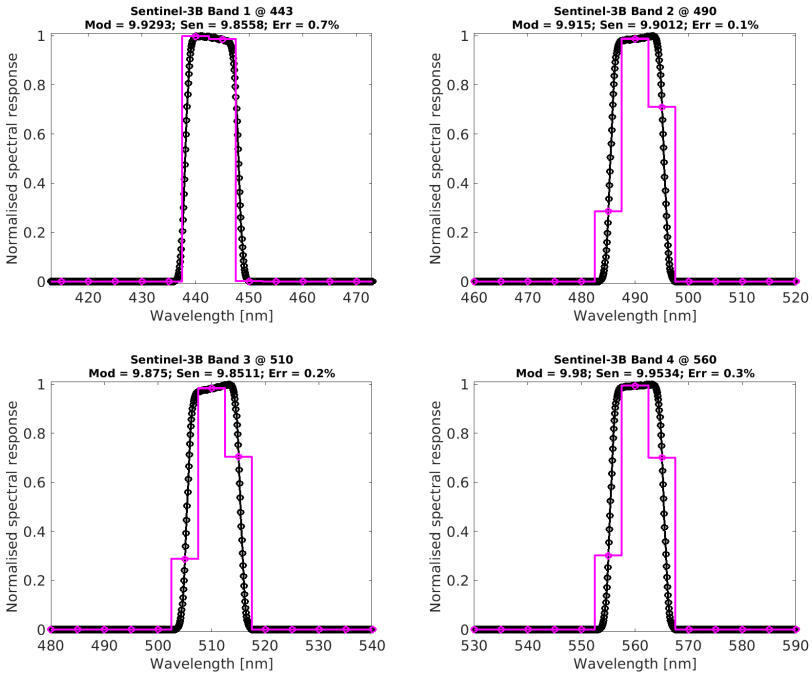

Figure 1: Spectral response curves for Sentinel-3B bands 3-6 determined at sensor calibration (black) and interpolated onto the model optical grid (pink). The error represents in difference in sensor band reflectance and model-calculated reflectance within that band for spectrally constant IOPs and surface light field.

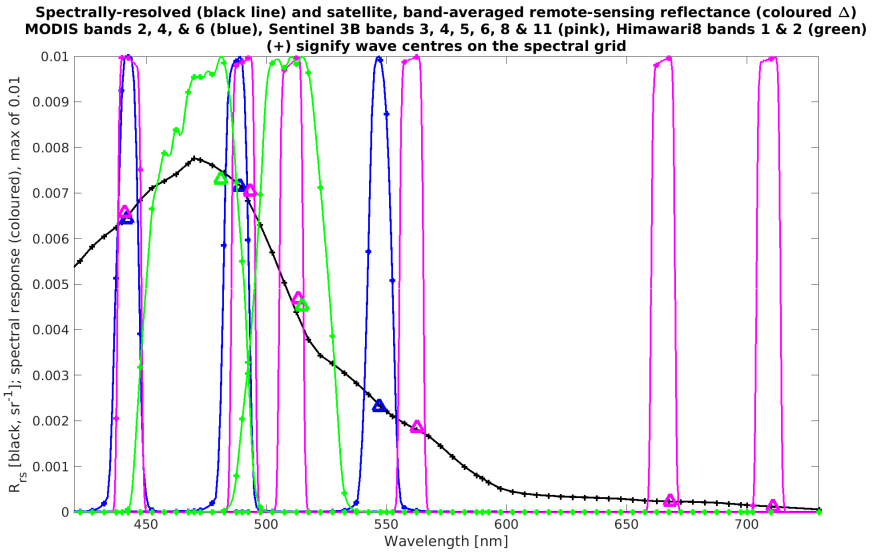

Figure 2: Spectrally-resolved (black line) and satellite, band-averaged remote-sensing reflectance (coloured Δ, plotted at the spectral response peak). Spectral response curves of MODIS bands 2, 4, & 6 (blue), Sentinel 3B bands 3, 4, 5, 6, 8 & 11 (pink), Himawari8 bands 1 & 2 (green) are shown, normalised to have a maximum of 0.01. (+) signifies wave centres on the spectral grid used for the band-averaged calculation.

3.4 Simulated hue angle and the Forel-Ule colour comparator scale

Hue is the 'colour' of light, and is often reported as an angle, the hue angle, around a colour wheel. Hue angle is calculated from weighting the primary colours (red, green and blue) by the standard human perception of colour (CIE 1931 standard colourimetric). The intensity of red and green are both normalised to the sum of red, green and blue, to provide a two dimensional quantification of colour. The two dimensions are then reduced to one by determining the angle generated by the division of the normalised red and green dimensions (y and x) relative to white (y_w, x_w, i.e. equal red/green/blue) (van der Woerd and Wernand, 2015), where the normalised values relative to white vary between -1 and 1. Thus the hue angle is calculated as $\alpha = \arctan(y - y_w, x - x_w)$ modulus 2π and varies along a continuum from blue (240°) to green (130°) to brown (20°).

One advantage of hue angle as a measure of normalised water leaving radiance is that it independent of saturation or intensity so is more likely to be consistent across sensor types and viewing conditions. Hue angle can be calculated directly from the remote-sensing reflectance at three or more wavelengths. We use the coefficients determined by van der Woerd and Wernand (2018) for Sentinel-2 MSI-60 to convert remote-sensing reflectance into the primary colours. Fig. 3 shows an image of hue angle for the GBR.

Another approach to quantifying colour is a 21-integer colour scale, called the Forel-Ule (FU) colour scale. Table 6 of Novoa et al. (2013) provides a conversion between the hue angle and the FU scale. Here the continuum is from blue (1) to brown (21) (Fig. 3). The FU scale has had broad, no expert use as an indicator of water colour and can be determined by simple colour card matching or smartphone apps.

3.5 Simulated true colour

True color images are often used in the geophysical sciences to provide a broad spatial view of a phenomenon such as cyclones, droughts or river plumes. Their strength lies in the human experience of natural colors that allows three 'layers' of information, and the interaction of these information streams, to be contained within one image. Spectacular true color images of, for example, the Great Barrier Reef (GBR), simultaneously depict reef, sand and mud substrates, sediment-laden river plumes and phytoplankton blooms. Further, the advection of spatially-variable suspended coloured constituents reveals highly-resolved flow patterns.

For these reasons and more, true color imagery has become a valued communication tool within both the geosciences and wider community. Here we demonstrate that the power of true colour images can be harnessed for interpreting geophysical models if the model output includes remote-sensing reflectance, or normalised water leaving radiance, at the red, green and blue wavelengths.

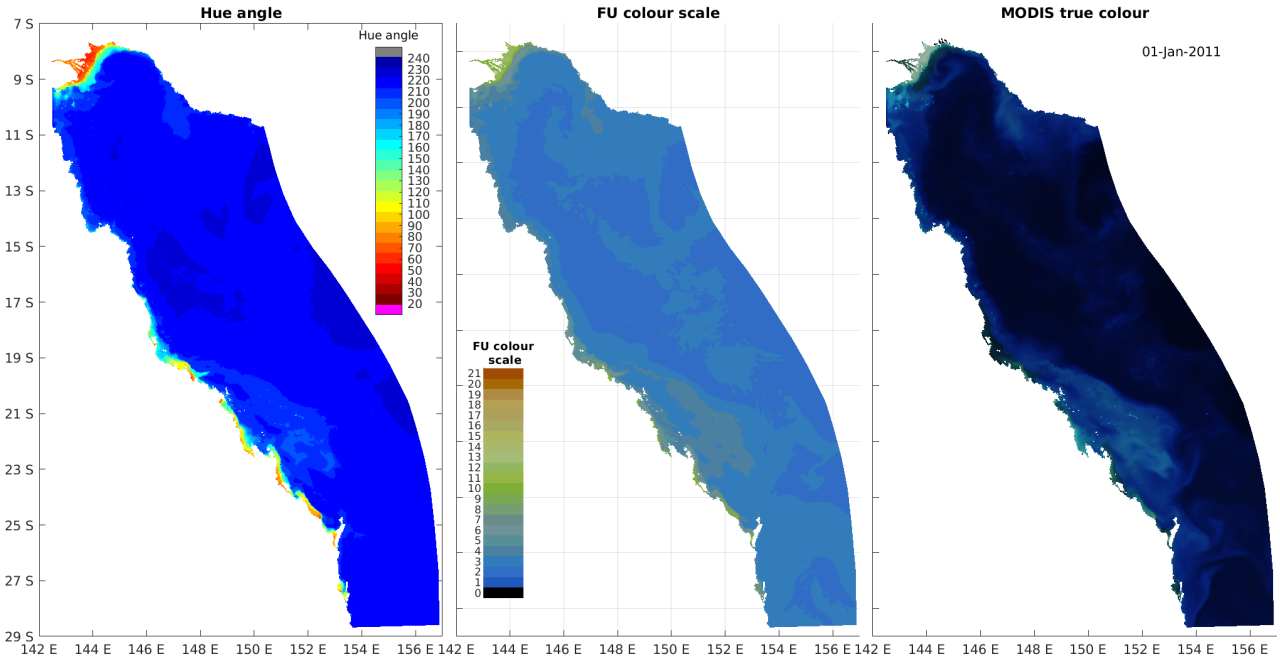

Figure 3: Simulated hue angle (left), Forel-Ule colour scale (centre) and MODIS true colour (right) calculated from simulated remote-sensing reflectance on the Great Barrier Reef on 1 Jan 2011.

In order to interpret simulated true colour images, a palette of true colours from the model optical relationships has been painted (Fig. 4), for varying values of water column CDOM, NAP and chlorophyll concentration. The green hues produced for varying IOPs are quite similar, demonstrating the difficulty in ocean colour analysis. The most obvious trend in the image is that Chl produces a greener hue than NAP (top panels vs bottom panels). The difference between increasing CDOM and chlorophyll (right panels vs left panels) is more subtle, which is a significant challenge in remote sensing of chlorophyll in high CDOM coastal waters (Schroeder et al., 2012).

The important role of scattering can be seen in Fig. 4. At low chl and / or NAP, the colour becomes dark at moderately low CDOM concentration. In reality CDOM is usually associated with either chlorophyll or NAP, hence natural waters rarely appear black.

As the model calculates remote-sensing reflectance at any wavelength, it is possible to reproduce simulated true colour images using the same algorithms as the MODIS processing (Fig. 5). The comparison of observed and modelled true colour images is particular insightful because the impact of multiple spectrally-distinct events (such as a sediment plume and a phytoplankton bloom) can be viewed on one image (Fig. 6). Furthermore, the colour match-up provides an intuitive and challenging test for parameterisation of the spectrally-resolved optical coefficients.

True colour images use intensity in the red, green and blue wavebands. We use the centre wavelengths of MODIS bands 1 (645 nm), 2 (555 nm) and 4 (470 nm). Simulated true colour image brightness is adjusted using the MODIS approach by linearly scaling the above surface remote-sensing reflectance at each wavelength so that the brightest band has an intensity of approximately 1. This requires multiplication of between 20 to 30. The scaled intensity is intensified in the darker bands by scaling [0 30 60 120 190 255]/255 onto [0 110 160 210 240 255]/255. The final image is rendered in MATLAB.

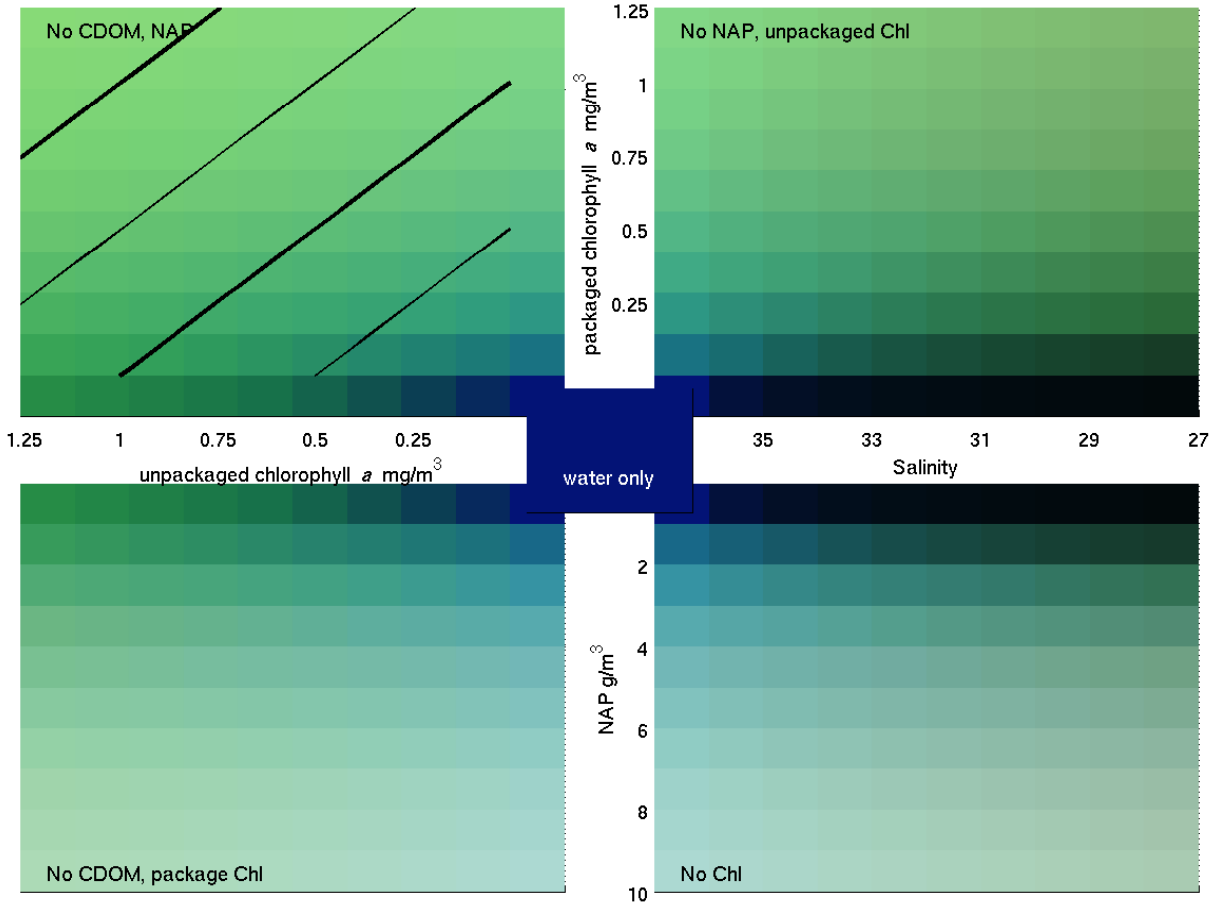

Figure 4: Palette of true colours from IOP relationships. The true colours are produced from the MODIS algorithm (Sec. 3.5), and IOP relationships in Sec. **??**. The centre box is the colour produced by clear water absorption and scattering alone. From the centre, moving right is increasing CDOM (as quantified by salinity), down is increasing NAP, and left and up are increasing chlorophyll in cells package by 0.35 and 0.73 respectively. The line contours in the top left panel are 0.5, 1, 1.5 and 2 mg Chl m^{-3}. Note that packaged chlorophyll is not plotted with NAP and unpackaged is not plotted with CDOM.

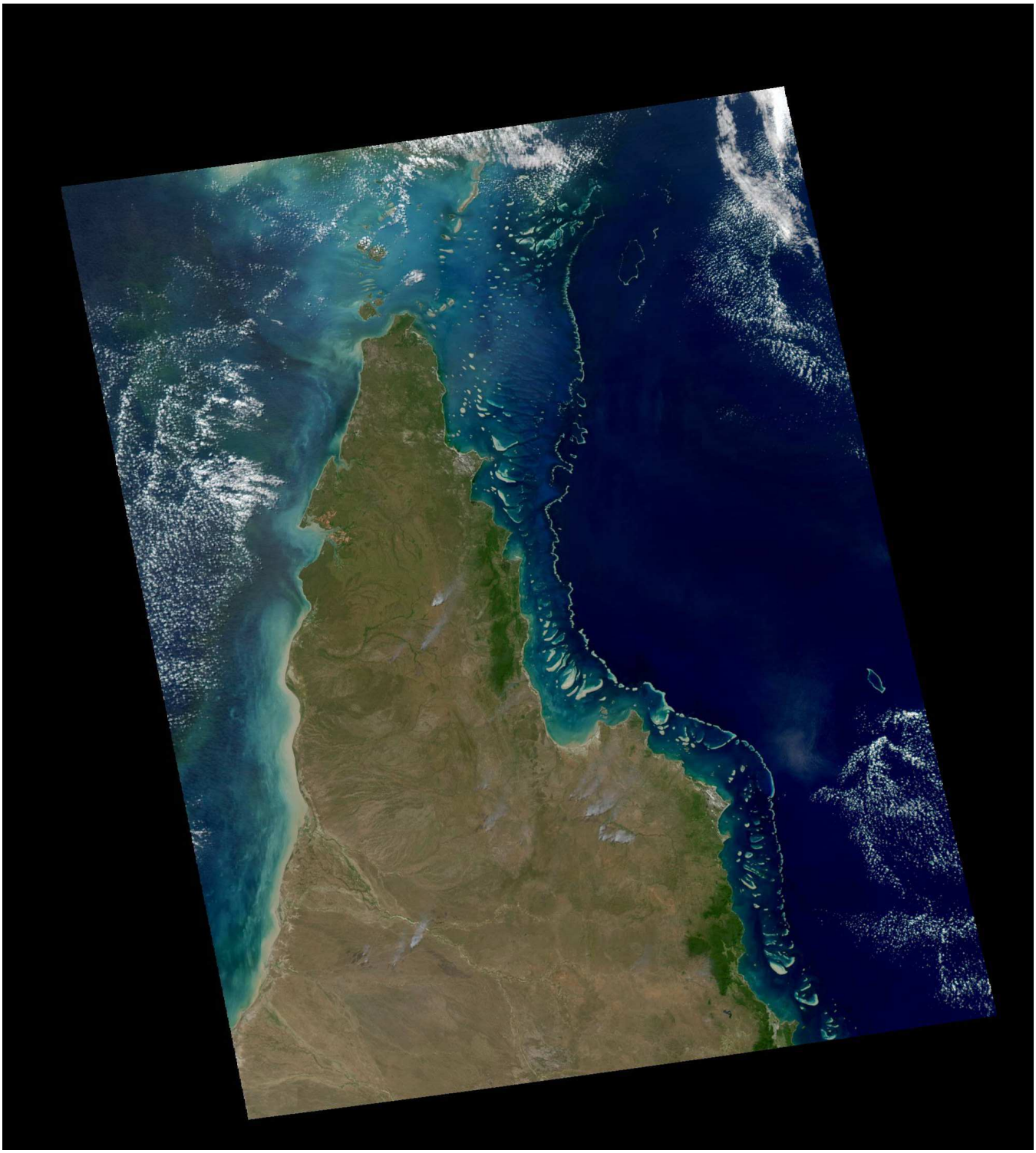

Figure 5: Observed true colour from MODIS using reflectance at 670, 555 and 470 nm.

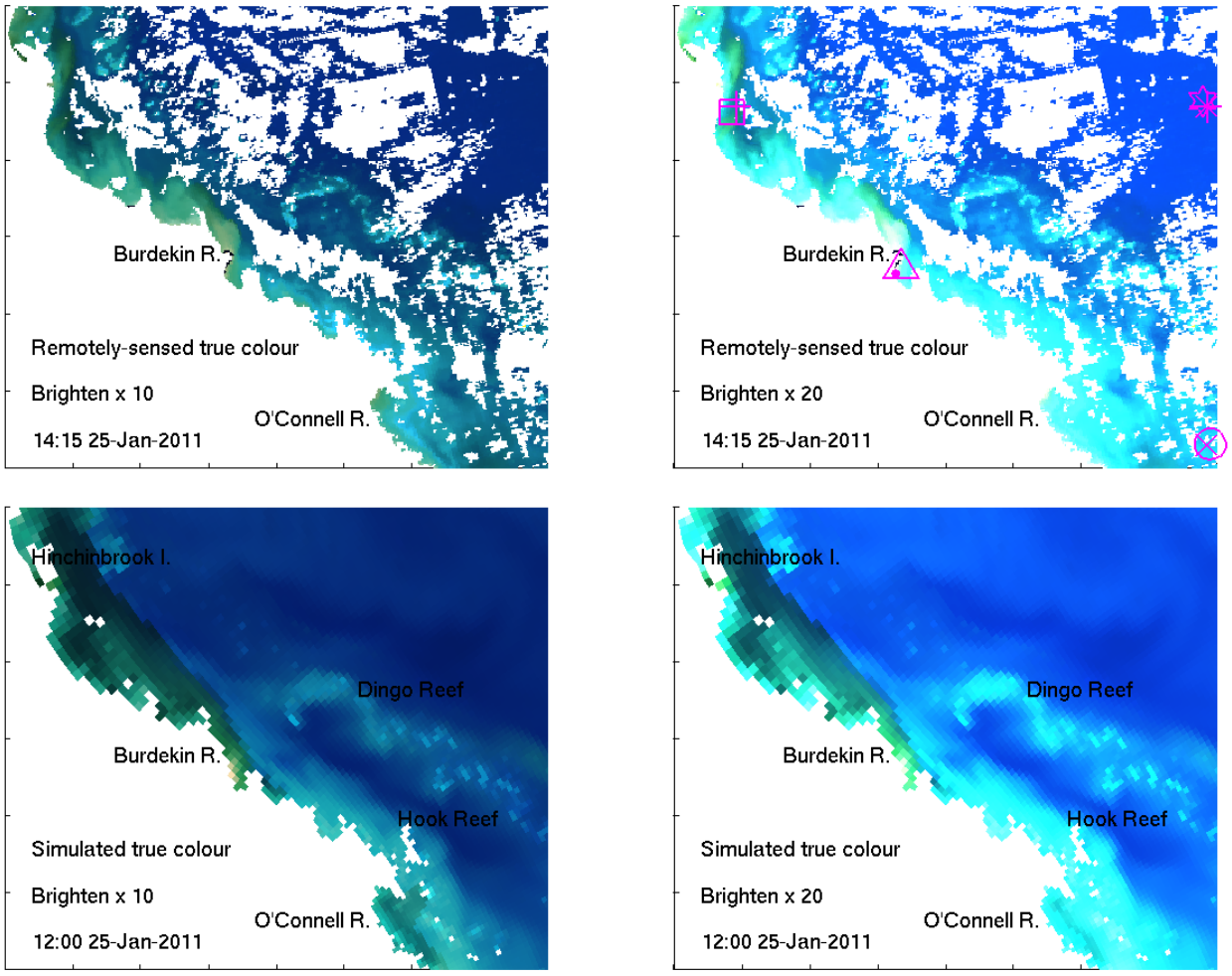

Figure 6: Observed (top) and simulated (bottom) true colour from simulated remote-sensing reflectance at 670, 555 and 470 nm in the GBR4 model configuration in the region of the Burdekin River. A brightening of 10 (left) and 20 (right) was applied for comparison.

3.6 Estimates of chlorophyll using the OC3 algorithm

The ratio of above-surface remote-sensing reflectance as a combination of three wavelengths, R', is given by:

$$R' = \log_{10}\left(\max\left[R_{rs,443}, R_{rs,488}\right]/R_{rs,551}\right) \tag{37}$$

The ratio R' is used in the MODIS OC3 algorithm to estimate surface chlorophyll, Chl_{OC3}, with coefficients from the 18 March 2010 reprocessing:

$$\mathrm{Chl}_{OC3} = 10^{0.283+R'(-2.753+R'(1.457+R'(0.659-1.403R')))} \tag{38}$$

obtained from `http://oceancolor.gsfc.nasa.gov/REPROCESSING/R2009/ocv6/`.

3.7 Estimates of vertical attenuation using the $K_{d,490}$ algorithm

The ratio of above-surface remote-sensing reflectance as a combination of two wavelengths, R', is given by:

$$R' = \log_{10}\left(R_{rs,488}/R_{rs,547}\right) \tag{39}$$

The ratio R' is used in the MODIS algorithm to estimate vertical attenuation at 490 nm, $K_{d,490}$, with coefficients from the 18 March 2010 reprocessing:

$$K_{d,490} = 10^{-0.8813+R'(-2.0584+R'(2.5878+R'(-3.4885-1.5061R')))} \tag{40}$$

obtained from `http://oceancolor.gsfc.nasa.gov/REPROCESSING/R2009/ocv6/`.

3.8 Estimates of particulate organic carbon using the POC algorithm

The ratio of above-surface remote-sensing reflectance as a combination of two wavelengths, R', is given by:

$$R' = \log_{10}\left(R_{rs,488}/R_{rs,555}\right) \tag{41}$$

The ratio R' is used in the MODIS algorithm to estimate concentration of particulate organic carbon, POC, with coefficients from the 18 March 2010 reprocessing:

$$POC = 308.3R'^{-1.639} \tag{42}$$

obtained from `http://oceancolor.gsfc.nasa.gov/REPROCESSING/R2009/ocv6/`.

3.9 Simulated turbidity from $b_{b,595}$

Turbidity is a measure of water clarity. The units of turbidity from a calibrated nephelometer are called Nephelometric Turbidity Units (NTU). Turbidity is often directly related to total suspended solids. However, as turbidity is measured optically (in the case of the three-wavelength Wetlabs sensor the scattering at 700 nm at a measured angle of 124°), it is better to produce a simulated turbidity - a calculation of what the optical model predicts an optical turbidity sensor would measure. Simulated turbidity, like simulated remote-sensing reflectance, is an example of "taking the model to the observations".

Thus, simulated turbidity (NTU) is given by:

$$\mathcal{T} = 47.02\,(b_{b,595} - 0.5 b_{b,clear,595}) + 0.13 \tag{43}$$

where $b_{b,595}$ is the backscattering coefficient at 595 nm, and the linear coefficient and offset were obtained from comparison of a BB9 backscattering sensor and a Wetlabs NTU at Lucinda Jetty, north Queensland. The coefficients are an empirical fit to the factory calibration of NTU standards. The clear water backscatter is removed because it was also removed in the output of the BB9. In practice

3.10 Estimates of total suspended matter using 645 nm

We use a local relationship between the remote-sensing reflectance at 645 nm, $R_{rs,645}$ [sr^{-1}], and total suspended matter, TSM (Petus et al., 2014):

$$TSM = \left(12450 R_{rs,645}^2 + 666 R_{rs,645} + 0.48\right)/1000 \tag{44}$$

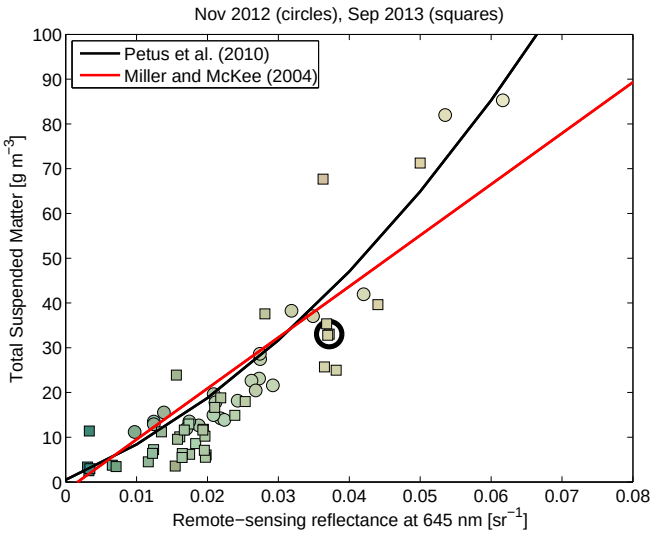

Figure 7: Relationship between the remote-sensing reflectance at 645 nm, $R_{rs,645}$, [sr^{-1}], and total suspended matter, TSM, in the samples taken during November 2012 (circles) and September 2013 (squares), compared to the empirical relationship of Petus et al. (2014) for the Bay of Biscay and Miller and McKee (2004) for the Mississippi. The symbols are coloured by true color, showing browner sites with higher TSM and remote-sensing reflectance. The black circle represents the site used for the model parameterisation of TSM optical properties.

3.11 Simulated fluorescence

The chlorophyll *a* molecule absorbs light at a range of wavelengths, and can, under certain circumstances, fluoresce strongly (Falkowski and Raven, 2007; Huot et al., 2005). As a result, active fluorescence is commonly used as a measure of chlorophyll *a* concentration. For this measurement, the stimulus for fluorescence comes from the sensor. For example, the Wetlabs ECOPuck emits light at 470 nm, and detects excitation at 695 nm. The fraction of the light that is returned depends primarily on the concentration of chlorophyll, but can also be affected by the size of the phytoplankton, through the packaging of pigments, and on the physiological state of the cells (Alvarez et al., 2017; Baird et al., 2013). As the model calculates spatially- and temporally- resolved measures of pigment packaging and cell physiology for each phytoplankton type, it is possible to calculate a new diagnostic, simulated fluorescence, that represents florescence that would be measured by a fluorometer exciting at 470 nm, measuring at 695 nm, and sampling a phytoplankton community with the properties (number, cell size, physiological state) of the phytoplankton in the model.

Simulated fluorescence uses the model predicted cell number, cell size, chlorophyll content, and the pigment-specific absorption coefficient at the excitation wavelength (470 nm, $\gamma = 0.03$ m^2 mg^{-1}) to calculate a simulated fluorescence. Specifically, the per unit of pigment absorption effectiveness, a^*, of a spherical cell r, pigment-specific absorption coefficient, γ, and intracellular pigment concentration c_i is given by:

$$a^* = \pi r^2 \left(1 - \frac{2(1-(1+2\rho)e^{-2\rho})}{4\rho^2}\right) / (n\gamma_{470} c_i V) \tag{45}$$

where $\rho = \gamma_{470} c_i r$, n is the concentration of cells and V is the cell volume ($4/3\pi r^3$). Because we are using the above equation to calculate the packaging effect, we sum the product $\gamma_{470} c_i$ for all pigments, recognising that the presence of any pigment can shade the chlorophyll a molecule.

Cell physiology also affects fluorescence. The photosystem II (PSII) fluorescences when light is absorbed by the cell, but not used for either photosynthesis or dissipated as heat by photoprotective pigments (called non-photochemical quenching, NPQ; see coral zooxanthellae photosystem model in (Baird et al., 2018)). To capture reduced fluorescence due to NPQ, we use the normalised carbon reserves of the cell, R^*_C.

The simulated fluorescence from all phytoplankton is given:

$$FL = CF \frac{3}{4} \sum_{p=1}^{P} a^*_p c_p \left(1 - 0.5 R^*_{C,p}\right) \tag{46}$$

where the sum is applied across all P cell types (small and large phytoplankton, *Trichodesmium*, microphytobenthos and dinoflagellates), c_p is the water column concentration of chlorophyll-a from each cell type, and CF is a calibration factor and depends on the initial factory calibration, which is

usually undertaken using a monoculture of a large diatom. The factor of 3/4 has been pulled out of CF to compare absorption cross-sections and volume specific attenuation (see Baird et al. (2013)). The term $(1 - 0.5R^*_C)$, accounts for the heat dissipation by the xanthophyll cycle, and takes a value of 1 when the carbon reserves are deplete (i.e. at depth in low light), and a value of 0.5 when the cells are carbon replete. The factor 0.5 accounts for the absorption of photosynthetic pigments even when the cell is energy replete, and can be thought of as the ratio of photoabsorbing pigments to xanthophyll pigments.

3.12 Simulated normalised fluorescence line height (nFLH)

In complex coastal waters, absorption in the blue is often dominated by CDOM, so band ratio algorithms like OC3M do not correlate well with *in situ* chlorophyll (Schroeder et al., 2012). An alternate, remotely-sensed, indirect measure of chlorophyll concentration is normalised fluorescence line height (nFLH, Behrenfeld et al. (2009)). nFLH is a measure of the light emitted by fluorescence at a red wavelength (678 nm for MODIS), as a result of solar radiation absorbed by photosynthetic pigments throughout the spectrum. Thus while simulated fluorescence described above (Sec. 3.11) is a measure of active fluorescence, nFLH is due to passive fluorescence. The passive fluorescence, PF (photon m^{-3}), at 678 nm due to absorption by P phytoplankton types is given by:

$$PF = \sum_{p=1}^{P} n_p \left(1 - 0.5R^*_{C,p}\right) R^*_C \frac{(10^9 hc)^{-1}}{A_V} \int \alpha E_{o,\lambda} \lambda d\lambda \tag{47}$$

where the term $\left(1 - 0.5R^*_{C,p}\right)$ is discussed in Sec. 3.11, the multiplication by R^*_C removes the component of absorption that is used for photosynthesis (that was not applied in Sec. 3.11 for simulated fluorescence due to the saturating pulse of the active fluorometer), and $E_{o,\lambda}$ is the scalar irradiance at wavelength λ [W m^{-2}], n_p is the concentration of cell type p [cell m^{-3}], and h, c and A_v are the Planck constant, speed of light in a vacuum and Avagadro number respectively.

The passive fluorescence is assumed to be emitted isotropically (equal in all directions) and is quantified per unit of volume. For the purposes of calculating the impact on remote-sensing reflectance, we need to consider only the upwelling component. The upwelling irradiance from a 1 m^3 spherical volume occurs through the area of a circle within the 1 m^3 volume, $\pi \left(\sqrt[3]{3/(4\pi)}\right)^2 \sim 1.21$ m^2, with only half of the volumetric radiance upwelled. Thus, the upwelling irradiance due to passive fluorescence is given by $\frac{PF}{2\pi\left(\sqrt[3]{3/(4\pi)}\right)^2}$.

To obtain remote-sensing reflectance we need to compare the upwelling component to downwelling irradance at 678 nm. This is already undertaken for the absorption and scattering of light in the balance of backscatter over absorption plus backscatter, u. Passive fluorescence at 678 nm adds to

this balance, with the component due at 678 nm:

$$u_{PF} = \frac{1}{2\pi \left(\sqrt[3]{3/(4\pi)}\right)^2} PF / \left(\frac{(10^9 hc)^{-1}}{A_V} 678 E_{o,678}\right) \tag{48}$$

This ratio of upwelling PF to downwelling solar radiation can then be added to u, the ratio of backscattering to absorption plus backscattering, at 678 nm (Eq. 17). The revised u then results in an updated $R_{rs,678}$, with the depth weighting based on the vertical attenuation coefficient.

Finally, nFLH is determined from the normalised water leaving irradiance (nLw) at the fluorescing band, and the bands either side of it. The term nLw is normalised to the sun zenith, $F_o = 148.097$ mW cm^{-2} μm^{-1},

$$nFLH = \frac{F_o}{\pi}\left(R_{rs,678} - \frac{70}{81}R_{rs,667} - \frac{11}{81}R_{rs,748}\right) \tag{49}$$

where π has units of sr^{-1} to convert between planar flux of nLw to a solid angle of remote-sensing reflectance (R_{rs}).

Note that passive fluorescence will contributes to the underwater light field in all directions, but because it is at 678 nm where there is strong absorption by clear water we have assumed that it does not lead to photosynthesis. Thus we have only considered the effect of passive fluorescence on $R_{rs,678}$ and therefore nFLH.

3.13 Secchi depth

Secchi depth is often calculated using:

$$Z_{SD} = 1.7/K_d \tag{50}$$

where K_d is a vertical attenuation of light, typically energy-weighted PAR. At a particular wavelength the constant varies from 1.7. In a recent study (Lee et al., 2015), it was shown that the constant has a value of approximately 1.0 when the colour of human perception of the disk surface is used as the wavelength. This varies in different waters, from 486 to 475 nm, as the water clarity improves. Even though this value is slightly bluer than 490 nm, we found a good match with observations for:

$$Z_{SD,490} = 1/K_{d,490} \tag{51}$$

The light level at the Secchi depth is $E_{SD,490} = E_{0,490}\exp(-Z_{SD,490}K_{d,490})$. Substituting Eq. 51, $E_{SD,490}/E_{0,490} = \exp(-1)$.

Depth-varying vertical attenuation. If $K_{d,490}$ varies with depth (as it does in the simulations), then the Secchi depth is found by looking for the layer in which $E_{SD,490}/E_{0,490}$ drops below $\exp(-1)$.

The top of this layer has a depth Z_{top}. Given a light level at the top of this layer of E_{top}, and an attenuation within the layer of $K_{d,490}$, the Secchi depth is given by:

$$Z_{SD,490} = Z_{top} + \log\left(\frac{\exp(-1)/E_{top}}{-K_{d,490}}\right) \tag{52}$$

Over 5000 measurements of Secchi depth have been undertaken in the GBR and used to develop a satellite algorithm for Secchi depth (Weeks et al., 2012). We adopt this approach to define a simulated remotely-sensed Secchi depth, Z_{SD}:

$$Z_{SD,sim,rs} = 10^{\left(\log_{10}\left(2.303/K_{d,490}\right)-0.529\right)/0.816} \tag{53}$$

where $2.303/K_{d,490}$ gives the 10 percent light depth and the empirical constants come from Weeks et al. (2012).

Finally these can be compared to the observed in situ Secchi depth, $Z_{SD,obs}$, and the remotely-sensed Secchi depth, $Z_{SD,rs}$.

3.14 Optical plume classification

Optical properties have been used to classify the extend of plumes (Devlin et al., 2013; Alvarez-Romero et al., 2013). Here we use a similar approach on simulated plumes. First we determine from observations the spectra of 6 standard plume classes (Fig. 8), as adopted by Alvarez-Romero et al. (2013). Using these standard plume classifications, we determine the dissimilarity between an observed or simulated spectra and the spectra of each standard class. The cosine dissimilarity between standard class c and the observed or simulated spectra, $S(c)$, is determined by:

$$S(c) = \cos^{-1}\left(\frac{\sum_{\lambda=1}^{W} R_{rs,c,\lambda} R_{rs,sim,\lambda}}{\sqrt{\sum_{\lambda=1}^{W} R_{rs,c,\lambda}^2}\sqrt{\sum_{\lambda=1}^{W} R_{rs,sim,\lambda}^2}}\right) \tag{54}$$

where $R_{rs,c,\lambda}$ is the remote-sensing reflectance of class c at wavelength λ, $R_{rs,sim,\lambda}$ is the remote-sensing reflectance of the simulation at wavelength λ and W is the number of wavelengths considered. The observed or simulated spectra is then assigned to the standard class c with the minimum dissimilarity, S, between the standard class and the observed or simulated spectra.

A simpler spectra matching scheme using the rms difference between the spectra is also employed.

Using this classification technique we can compare the extent of plumes in an observed scene (Fig. 9 left), and a simulated scene (Fig. 9 right) of the same day. The areal extent of the observed and simulated plume classes can also be calculated, noting that the observed area is less due to clouds.

As a metric of the recent history of plume exposure, we propose a metric the plume exposure, $\mathcal{P}$, which is given by:

$$\mathcal{P} = \int_{t-t_{c<6}}^{t} (1/c)\, dt \tag{55}$$

where c is the plume class determined from Eq. 54. The plume exposure is calculated for each model grid cell. The metric is calculated from the most recent time that c for a grid cell was less than 6 (i.e. impacted by a plume class 1, 2, 3, 4 or 5). The metric is a weighted-running mean, such that exposure to plume class 1 for 10 days would give a value of 10, plume class 2 for 10 days 5, plume class 3 for 10 days would give 10/3 etc.

An additional concept is the annual plume extent, or the mean plume area over the year.

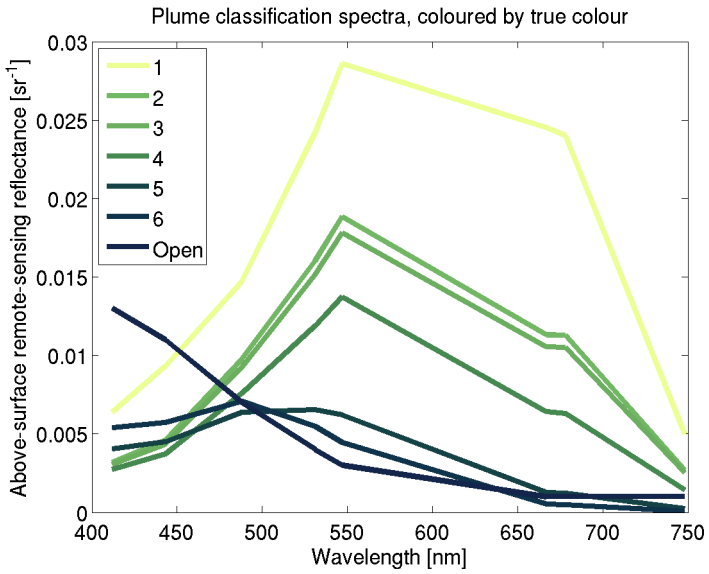

Figure 8: Spectra of each of the optical plume classifications (1-6) and the open ocean. The area in km^2 for each plume class within the region plotted is given on the left for both the observed and simulated classes.

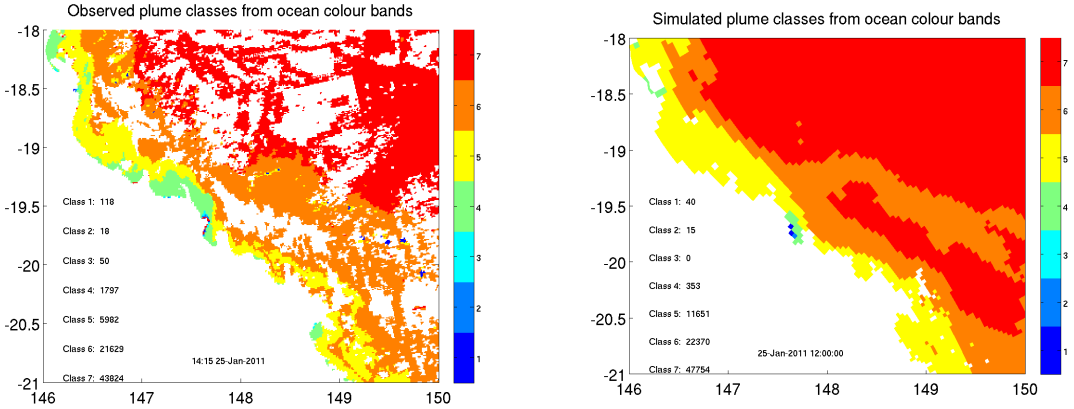

Figure 9: Observed and simulated optical plume classification on the 25 Jan 2011 in the Burdekin River region. See Fig. 8 for spectra of individual classes.

Description	Calculation	Application
Monthly bottom light (eqival. to daily dose]	1 hourly running-mean $\frac{1}{\tau}\int_0^t E_{d,\lambda,t}\exp(-(t-t')/\tau)dt'$ [mol m^{-2} d^{-1}]	seagrass viability
Aragonite dissolution exposure	$\int_{t-t_{\Omega<3}}^{t}(3-\Omega)\,dt'$ reset time 1 day, [unit days]	acidification stress
Monthly net calcification rate	1 hourly running-mean $\frac{1}{\tau}\int_0^t g_{net,t}\exp(-(t-t')/\tau)dt'$	calcification index coral accretion
Temperature exposure (degree heating weeks)	$\int_{t-t_{T>T_{clim}}}^{t}(T-T_{clim})\,dt'$ rest time 7 day, [°C weeks]	thermal coral bleaching
Weekly inorganic N uptake by corals	1 hourly running-mean $\frac{1}{\tau}\int_0^t G_t\exp(-(t-t')/\tau)dt'$	oxidative stress
Salinity exposure	$\int_{t-t_{S<28}}^{t}(28-S)\,dt'$ reset time 1 day, [PSU days]	freshwater coral bleaching
Weekly net deposition rate (sinking / resuspension / diffusion)	1 hourly running-mean $\frac{1}{\tau}\int_0^t D_t\exp(-(t-t')/\tau)dt'$ [cm d^{-1}]	coral smothering
Hypoxic exposure	$\int_{t-t_{[O_2]<2000}}^{t}(2000-[O_2])\,dt$ rest time 1 hour, [mg O m^{-3} d^{-1}]	low oxygen stress
Weekly bottom light attenuation (approx. from 490 nm)	1 hourly running-mean $\frac{1}{\tau}\int_0^t K_{d,490,t}\exp(-(t-t')/\tau)dt'$ [m^{-1}]	predator visibility prey behaviour
Remote-sensing reflectance R_{rs}	see Section **??** 412, 443, 488, 531, 547, 648, 667, 748 nm	comparison with ocean colour products
MODIS algorithms - Kd, OC3, TSS, POC - Kd, OC3, TSS, POC	empirical algorithms using remote-sensing reflectance	comparison with ocean colour products
Simulated true colour	RGB additive colour model using remote-sensing reflectance	water quality non-expert communication
Plume classification (1-6) + clear water	categorical from spectra matching using RMS errors on OC bands 1-7	plume extent

Table 11: Diagnostic variables. In addition to 60+ state variables, derived diagnostic variables have been developed in consultation with researchers and managers that provide metrics for improve understanding and application. For those metrics with a time scale, τ, see Sec. 3.15.1.

3.15 Diagnostic variables calculates by `tracerstat`.

The EMS software provides a library call `tracerstat` that calculates a diagnostic variable from a combination of prognostics and diagnostic variables, and can be the result of an integration in space or time. The EMS manual describes some of these. Here we concentration on options used in the BGC model.

3.15.1 Running mean

For model output, the calculation of a mean over time is problematic if not all values from which the mean is to be calculated are archived. A good example of this light, where a midday output is useless as a daily mean. To overcome this, we introduce a running mean calculated from the weighted sum of the running mean at the previous time step, and the present value of the variable. Thus, for a 24 hour running mean, with outputs every hour, the running mean for downwelling irradiance, $\overline{E_d}$, is given by:

$$\overline{E_{d,t}} = \frac{23}{24}\ \overline{E_{d,t-1}} + \frac{1}{24}\, E_{d,t} \tag{56}$$

As this procedure is applied at each timestep, the running mean can be written as a time-integral with an exponential decay of the importance of earlier values:

$$\overline{E_{d,t}} = \frac{1}{\tau}\int_0^t E_{d,t}\exp(-(t-t')/\tau)dt' \tag{57}$$

where the running mean coefficient, τ represents an exponential decay time. Thus for a weekly running average, the impact of the value 1 week earlier on the running average is $100 \times \exp(-1)$, or 37 % of the impact of the present value. Or 63.2 % of the value is based on the last week, 86.5 % on the last two weeks.

4 Acknowledgements

Many scientists and projects have contributed resources and knowhow to the development of this model over 15+ years. For this dedication we are very grateful.

Those who have contributed to the numerical code include (CSIRO unless stated):

Mike Herzfeld, Philip Gillibrand, John Andrewartha, Farhan Rizwi, Jenny Skerratt, Mathieu Mongin, Mark Baird, Karen Wild-Allen, John Parlsow, Emlyn Jones, Nugzar Margvelashvili, Pavel

Sakov, Jason Waring, Stephen Walker, Uwe Rosebrock, Brett Wallace, Ian Webster, Barbara Robson, Scott Hadley (University of Tasmania), Malin Gustafsson (University of Technology Sydney, UTS), Matthew Adams (University of Queensland, UQ).

Collaborating scientists include:

Bronte Tilbrook, Andy Steven, Thomas Schroeder, Nagur Cherukuru, Peter Ralph (UTS), Russ Babcock, Kadija Oubelkheir, Bojana Manojlovic (UTS), Stephen Woodcock (UTS), Stuart Phinn (UQ), Chris Roelfsema (UQ), Miles Furnas (AIMS), David McKinnon (AIMS), David Blondeau-Patissier (Charles Darwin University), Michelle Devlin (James Cook University), Eduardo da Silva (JCU), Julie Duchalais, Jerome Brebion, Leonie Geoffroy, Yair Suari, Cloe Viavant, Lesley Clementson (pigment absorption coefficients), Dariusz Stramski (inorganic absorption and scattering coefficients), Erin Kenna, Line Bay (AIMS), Neal Cantin (AIMS) and Luke Morris (AIMS).

Funding bodies: CSIRO Wealth from Oceans Flagship, Gas Industry Social & Environmental Research Alliance (GISERA), CSIRO Coastal Carbon Cluster, Derwent Estuary Program, INFORM2, eReefs, Great Barrier Reef Foundation, Australian Climate Change Science Program, University of Technology Sydney, Department of Energy and Environment, Integrated Marine Observing System (IMOS), National Environment Science Program (NESP TWQ Hub).

References

Alvarez, E., Nogueira, E., Lopez-Urrutia, A., 2017. *In vivo* single-cell fluorescence and size scaling of phytoplankton chlorophyll content. App. Env. Microbiol. 83, e03317–16.

Alvarez-Romero, J. G., Devlin, M., da Silva, E. T., Petus, C., Ban, N. C., Pressey, R. L., Kool, J., Roberts, J. J., Cerdeira-Estrada, S., Wenger, A. S., Brodie, J., 2013. A novel approach to model exposure of coastal-marine ecosystems to riverine flood plumes based on remote sensing techniques. J. Enviro. Manage. 119, 194–207.

Baird, M. E., Cherukuru, N., Jones, E., Margvelashvili, N., Mongin, M., Oubelkheir, K., Ralph, P. J., Rizwi, F., Robson, B. J., Schroeder, T., Skerratt, J., Steven, A. D. L., Wild-Allen, K. A., 2016. Remote-sensing reflectance and true colour produced by a coupled hydrodynamic, optical, sediment, biogeochemical model of the Great Barrier Reef, Australia: comparison with satellite data. Env. Model. Softw. 78, 79–96.

Baird, M. E., Mongin, M., Rizwi, F., Bay, L. K., Cantin, N. E., Soja-Woźniak, M., Skerratt, J., 2018. A mechanistic model of coral bleaching due to temperature-mediated light-driven reactive oxygen build-up in zooxanthellae. Ecol. Model. 386, 20–37.

Baird, M. E., Ralph, P. J., Rizwi, F., Wild-Allen, K. A., Steven, A. D. L., 2013. A dynamic model of the cellular carbon to chlorophyll ratio applied to a batch culture and a continental shelf ecosystem. Limnol. Oceanogr. 58, 1215–1226.

Baird, M. E., Timko, P. G., Suthers, I. M., Middleton, J. H., 2006. Coupled physical-biological modelling study of the East Australian Current with idealised wind forcing. Part I: Biological model intercomparison. J. Mar. Sys. 59, 249–270.

Baird, M. E., Wild-Allen, K. A., Parslow, J., Mongin, M., Robson, B., Skerratt, J., Rizwi, F., Soja-Woźnaik, M., Jones, E., Herzfeld, M., Margvelashvili, N., Andrewartha, J., Langlais, C., Adams, M. P., Cherukuru, N., Gustafsson, M., Hadley, S., Ralph, P. J., Rosebrock, U., Schroeder, T., Laiolo, L., Harrison, D., Steven, A. D. L., 2020. CSIRO Environmental Modelling Suite (EMS): Scientific description of the optical and biogeochemical models (vB3p0). Geoscientific Model Development 13, 4503–4553.

Behrenfeld, M. J., Westberry, T. K., Boss, E. S., O'Malley, R. T., Siegel, D. A., Wiggert, J. D., Franz, B. A., McClain, C. R., Feldman, G. C., Doney, S. C., Moore, J. K., Dall'Olmo, G., Milligan, A. J., Lima, I., Mahowald, N., 2009. Satellite-detected fluorescence reveals global physiology of ocean phytoplankton. Biogeosciences 6 (5), 779–794.

Brando, V. E., Dekker, A. G., Park, Y. J., Schroeder, T., 2012. Adaptive semianalytical inversion of ocean color radiometry in optically complex waters. Applied Optics 51, 2808–2833.

Dekker, A. G., Phinn, S. R., Anstee, J., Bissett, P., Brando, V. E., Casey, B., Fearns, P., Hedley, J., Klonowski, W., Lee, Z. P., Lynch, M., Lyons, M., Mobley, C., Roelfsema, C., 2011. Intercomparison of shallow water bathymetry, hydro-optics, and benthos mapping techniques in Australian and Caribbean coastal environments. Limnol. Oceanogr.: Methods 9, 396–425.

Devlin, M., da Silva, E., Petus, C., Wenger, A., Zeh, D., Tracey, D., Alvarez-Romero, J., Brodie, J., 2013. Combining in-situ water quality and remotely sensed data across spatial and temporal scales to measure variability in wet season chlorophyll-a: Great Barrier Reef lagoon (Queensland, Australia). Ecological Processes 2, 31.

Eyre, B. D., Cyronak, T., Drupp, P., Carlo, E. H. D., Sachs, J. P., Andersson, A. J., 2018. Coral reefs will transition to net dissolving before end of century. Science 359, 908–911.

Falkowski, P. G., Raven, J. A., 2007. Aquatic Photosynthesis, 2nd Edition. Blackwell Science.

Goddijn-Murphy, L., Woolf, D. K., Marandino, C., 2012. Space-based retrievals of air-sea gas transfer velocities using altimeters: Calibration for dimethyl sulfide. J. Geophys. Res. 117, C08028.

Hamilton, L. J., 2001. Cross-shelf colour zonation in northern Great Barrier Reef lagoon surficial sediments. Aust. J. Earth Sci. 48, 193–200.

Huot, Y., Brown, C. A., Cullen, J. J., 2005. New algorithms for MODIS sun-induced chlorophyll fluorescence and a comparison with present data products. Limnol. Oceanogr. Methods 3, 108–130.

Jackson, R. L., Gabric, A. J., Matrai, P., Woodhouse, M. T., Cropp, R., Jones, G. B. e. a., 2020a. Parameterizing the impact of seawater temperature and irradiance on dimethylsulfide (DMS) in the Great Barrier Reef and the contribution of coral reefs to the global sulfur cycle, journal = Journal of Geophysical Research: Oceans 126, e2020JC016783.

Jackson, R. L., Gabric, A. J., Woodhouse, M. T., Swan, H. B., Jones, G. B., Cropp, R., Deschaseaux, E. S. M., 2020b. Coral reef emissions of atmospheric dimethylsulfide and the influence on marine aerosols in the southern Great Barrier Reef, Australia. Journal of Geophysical Research: Atmospheres 125 (7), e2019JD031837.

Lee, Z., Carder, K. L., Arnone, R. A., 2002. Deriving inherent optical properties from water color: a multiband quasi-analytical algorithm for optically deep waters. Applied Optics 41, 5755–5772.

Lee, Z., Shang, S., Hu, C., Du, K., Weidermann, A., Hou, W., Lin, J., Lin, G., 2015. Secchi disk depth: A new theory and mechanistic model for underwater visibility. Remote sensing of environment 169, 139–149.

Leiper, I., Phinn, S., Dekker, A. G., 2012. Spectral reflectance of coral reef benthos and substrate assemblages on Heron Reef, Australia. Int. J. of Rem. Sens. 33, 3946–3965.

Macdonald, H. S., Baird, M. E., Middleton, J. H., 2009. The effect of wind on continental shelf carbon fluxes off southeast Australia: a numerical model. J. Geophys. Res. 114, C05016,doi:10.1029/2008JC004946.

Margvelashvili, N., 2009. Stretched Eulerian coordinate model of coastal sediment transport. Computer Geosciences 35, 1167–1176.

Miller, R. L., McKee, B. A., 2004. Using modis terra 250 m imagery to map concentrations of suspended matter in coastal waters. Remote Sens. Environ. 93, 259–266.

Mishchenko, M. I., Travis, L. D., Lacis, A. A., 2002. Scattering, Absorption and Emission of Light by Small Particles. Cambridge University Press.

Mongin, M., Baird, M. E., Tilbrook, B., Matear, R. J., Lenton, A., Herzfeld, M., Wild-Allen, K. A., Skerratt, J., Margvelashvili, N., Robson, B. J., Duarte, C. M., Gustafsson, M. S. M., Ralph, P. J., Steven, A. D. L., 2016. The exposure of the Great Barrier Reef to ocean acidification. Nature Communications 7, 10732.

Monsen, N., Cloern, J., Lucas, L., Monismith, S. G., 2002. A comment on the use of flushing time, residence time, and age as transport time scales. Limnol. Oceanogr. 47, 1545–1553.

Novoa, S., Wernand, M. R., van der Woerd, J. J., 2013. The Forel-Ule scale revisited spectrally: preparation protocol, transmission measurements and chromaticity. Journal of the European Optical Society - Rapid publications 8, 13057.

Petus, C., Marieua, V., Novoac, S., Chust, G., Bruneau, N., Froidefond, J.-M., 2014. Monitoring spatio-temporal variability of the Adour River turbid plume (Bay of Biscay, France) with MODIS 250-m imagery. Cont. Shelf Res. 74, 35–49.

Reichstetter, M., Fearns, P. R., Weeks, S. J., McKinna, L. I., Roelfsema, C., Furnas, M., 2015. Bottom reflectance in ocean color satellite remote sensing for coral reef environments. Remote Sens. 7, 15852.

Roelfsema, C. M., Phinn, S. R., 2012. Spectral reflectance library of selected biotic and abiotic coral reef features in Heron Reef. Tech. rep., Centre for Remote Sensing and Spatial Information Science, School of Geography, Planning and Environmental Management, University of Queensland, Brisbane, Australia, doi:10.1594/PANGAEA.804589.

Saltzman, E., King, D., Holmen, K., Leck, C., 1993. Experimental determination of the diffusion coefficient of dimethylsulfide in water. J. Geophys. Res. 98(C9), 16481–16486.

Schroeder, T., Devlin, M. J., Brando, V. E., Dekker, A. G., Brodie, J. E., Clementson, L. A., McKinna, L., 2012. Inter-annual variability of wet season freshwater plume extent into the Great Barrier Reef lagoon based on satellite coastal ocean colour observations. Mar. Pollut. Bull. 65, 210–223.

Soja-Woźniak, M., Baird, M. E., Schroeder, T., Qin, Y., Clementson, L., Baker, B., Boadle, D., Brando, V., Steven, A., 2019. Particulate backscattering ratio as an indicator of changing particle composition in coastal waters: observations from Great Barrier Reef waters. J. Geophys. Res. (Oceans) 124.

Vaillancourt, R. D., Brown, C. W., Guillard, R. R. L., Balch, W. M., 2004. Light backscattering properties of marine phytoplankton: relationship to cell size, chemical composition and taxonomy. J. Plank. Res. 26, 191–212.

van der Woerd, H. J., Wernand, M. R., 2015. True colour classification of natural waters with medium-spectral resolution satellites: SeaWiFS, MODIS, MERIS and OLCI. Sensors 15, 25663–25680.

van der Woerd, H. J., Wernand, M. R., 2018. Hue-angle product for low to medium spatial resolution optical satellite sensors. Remote Sensing 10, 180.

Wanninkhof, R., 1992. Relationship between wind speed and gas exchange over the ocean. J. Geophys. Res. 97 (C5), 7373–7382.

Wanninkhof, R., McGillis, W. R., 1999. A cubic relationship between air-sea CO_2 exchange and wind speed. Geophys. Res. Letts. 26, 1889–1892.

Weeks, S., Werdell, P. J., Schaffelke, B., Canto, M., Lee, Z., Wilding, J. G., Feldman, G. C., 2012. Satellite-derived photic depth on the Great Barrier Reef: spatio-temporal patterns of water clarity. Remote Sens. 4, 3781–3795.

A Additions to B3p0

The following changes in the model equations were made between versions B2p0 and B3p0:

- Optical properties of carbonate particles (absorption, scattering and backscattering coefficients) are introduced using observations from the Lucinda Jetty Coastal Observatory.
- Spectrally-resolved phytoplankton backscattering replaces a wavelength-independent value.
- Coral bleaching processes added using new variables (Coral N, P, C reserves, xanthophyll photosynthetic and heat dissipating pigments, oxidised, reduced and inhibited reaction centres, reactive oxygen species), parameter values (ROS_threshold) and diagnostics (Rubisco activity, bleaching rate) following (Baird et al., 2018).

- Coral heterotrophic feeding fixed: reserves from grazed phytoplankton now returned to water column.
- New diagnostic variables included in optical model: simulated fluorescence, simulated turbidity, simulated normalised fluorescence line height, simulated Secchi depth, downwelling light on z-level interfaces, SWR_bot_abs (the PAR weighted bottom absorption calculated by the model), OC4Me - chlorophyll algorithm for MERIS and Sentinel satellites.
- Optical code now has options of spectral absorption coefficients calculated from mass-specific absorption laboratory experiments.
- Apply a relationship between aragonite saturation and sediment carbonate dissolution (Eyre et al., 2018).
- Spectrally-resolved light absorption by microphytobenthos in the sediment porewaters.
- Mass balance for oxygen includes oxygen atoms in nitrate, with stoichiometry changed for photosynthesis / respiration.
- In the model description, energy reserves are more correctly referred to as carbon reserves.
- Quadratic term for seagrass mortality.
- Remineralisation rate of phosphorus has a separate rate to that of C and N, requiring 2 new parameters (Φ_{RD_P}, Φ_{DOM_P}).
- Introduced new sediment-water exchange rate diagnostic variables for C, N, P, and O.

B Additions to B3p1

C Additions to B3p2